Supporting Information for

The Southern Ocean carbon cycle 1985-2018: mean, seasonal cycle, trends and storage

Judith Hauck, Luke Gregor, Cara Nissen, Lavinia Patara, Mark Hague, N. Precious Mongwe, Seth Bushinsky, Scott C. Doney, Nicolas Gruber, Corinne Le Quere, Manfredi Manizza, Matthew Mazloff, Pedro M. S. Monteiro, Jens Terhaar

See main text for affiliations.

Contents of this file

Introduction

- The supplementary material contains additional information and analysis. In particular, we present additional analysis, resolved to show results of individual data sets and further separation into Atlantic, Pacific and Indian Ocean sectors of the Southern Ocean.

Text S1. Linear CO_2 flux trends in the control simulation

In the whole Southern Ocean, the linear trend in simulation B (Figure S1) is smaller than 10 TgC yr^{-1} decade^{-1} for 10 out of the 14 models; larger than 10 TgC yr^{-1} decade^{-1} for the other four (maximum 55 TgC yr^{-1} decade^{-1}). Overall, the trend in simulation B is thus small compared to the mean fluxes in simulation A.

Text S2. Non steady state component of ΔC_{ant} accumulation rates

In Figures 11-13 we show the steady state ΔC_{ant} for OCIMv2021 and two GOBMs (CNRM, and MPIOM-HAMOCC), since it is the only one available, whereas the total ΔC_{ant} (i.e. the sum of the steady state and non-steady components) is shown for the other data

sets. This warrants a closer inspection at the non-steady ΔC_{ant} (Fig. S3) in relation to the steady ΔC_{ant}. Indeed, total ΔC_{ant} accumulation rates between 1994-1007 patterns may be affected by decadal changes in ocean circulation occurring over that period, which would affect its non-steady component (but not its steady component). As it can be seen from Fig. S3, ΔC_{ant}^{ns} is around 10-20% of the total ΔC_{ant} (Fig. S4). The spatial patterns of ΔC_{ant}^{ns} are quite diverse among GOBMs (despite having an overall tendency towards increased ΔC_{ant} uptake in the Weddell Sea), which is surprising considering that GOBMs are forced by similar atmospheric reanalysis products. It can be concluded that other factors, such as model internal variability and the individual strategy to perform a steady-state simulation, play a role in driving ΔC_{ant}^{ns}.

Text S3. Computation of annual MLD diagnostic

Given its important role in ventilating the deep ocean (Morrison et al., 2022), we include here an assessment of mixed layer depth (MLD) across different GOBMs. In addition to the user-defined fixed-threshold September MLD provided by all of GOBMs, we additionally computed MLDs based on the interior temperature and salinity values using a variable density threshold method (Holte et al., 2017). Because, following the RECCAP-2 protocol, most GOBMs provided only annually-averaged temperature and salinity values, we call this diagnostic an annual MLD diagnostic. Monthly means would have been the preferred choice, considering the large seasonal variations in the upper ocean temperature and salinity, but this diagnostic has the advantage of being computed uniformly across all GOBMs and of using a variable density threshold, which has been shown to provide a more realistic picture especially at high latitudes (Holte et al., 2017). 3D monthly fields were only available for two hindcast models (NEMO-PlankTOM12 and CCSM-WHOI) and for the observed World Ocean Atlas 2018 (WOA18 climatology). An analysis of the impact of using annual means instead of monthly means of temperature and salinity, shows an underestimation of annual MLD diagnostic with respect to the monthly MLD diagnostic of around 45%-50% but no significant differences in spatial patterns.

Text S4. Composite analysis of "GOBMs high" and "GOBMs low"

To gain a better understanding of the factors driving the inter-model spread in ΔC_{ant} accumulation rates, we analyzed composites for GOBMs overestimating (hereafter "GOBMs high", Figure 11c) and underestimating (hereafter "GOBMs low", Figure 11d) ΔC_{ant} with respect to the average of the two observationally-constrained estimates. A consistent pattern of higher ΔC_{ant} accumulation rates in the "GOBMs high" with respect to "GOBMs low" emerges (Fig. 11c,d, Figure S4). Composite anomalies with respect to the multi-model-mean of different physical variables (Fig. S17) can help interpret the drivers of the different ΔC_{ant} accumulation rates in "GOBMs high" and "GOBMs low". "GOBMs high" consistently show positive anomalies of C_{ant} air-sea fluxes throughout the Southern Ocean (except for some areas around Antarctica), associated with higher-than-average sea surface salinity (SSS) and deeper mixing in the STSS and SPSS biomes. Mixing anomalies are distributed more uniformly when using the annual MLD diagnostic (Text S3) than when using the user-defined September MLD. The clear dependence of

C_{ant} air-sea fluxes on SSS in the STSS and SPSS biomes is in line with Terhaar et al. (2021) and with results from the Evaluation Chapter of RECCAP-2 (Terhaar et al., 2023) where a tight relationship is found between C_{ant} air-sea fluxes and SSS averaged between the Polar Front (approximately the southern edge of the SPSS biome) and the Subtropical Front (approximately the northern edge of the STSS biome). Interestingly, "GOBMs high" models have lower-than-average SSS in the ICE biome, possibly because of thicker sea ice (Fig. S17), which impedes the formation of polynyas and associated brine rejection. By construction, the anomalies of "GOBMs low" provide a specular picture with respect to "GOBMs high".
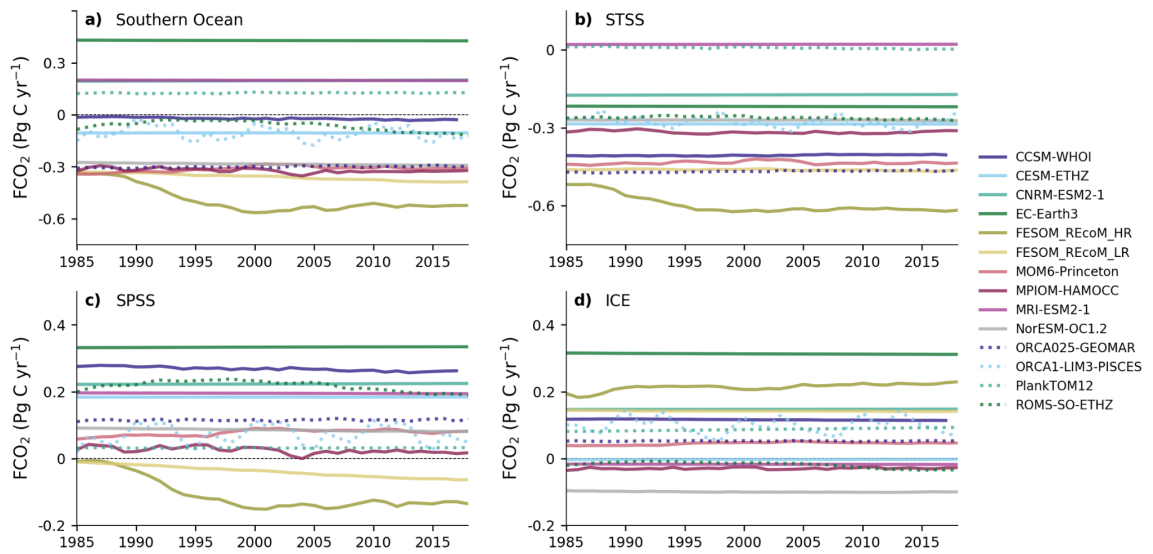
Figure S1. CO_2 flux in simulation B (control) for each individual GOBM for the (a) Southern Ocean, (b) STSS, (c) SPSS, and (d) ICE biomes.
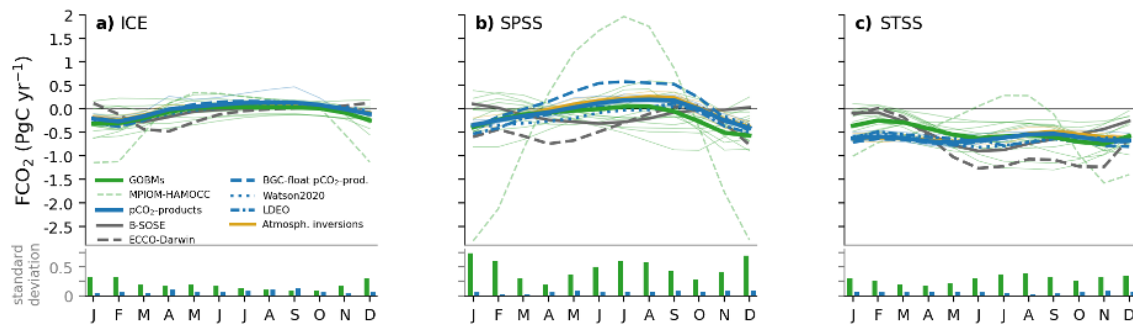
Figure S2. Same as Figure 6a-c, but with MPIOM-HAMOCC included. Note the different y-axes scales compared to Figure 6.
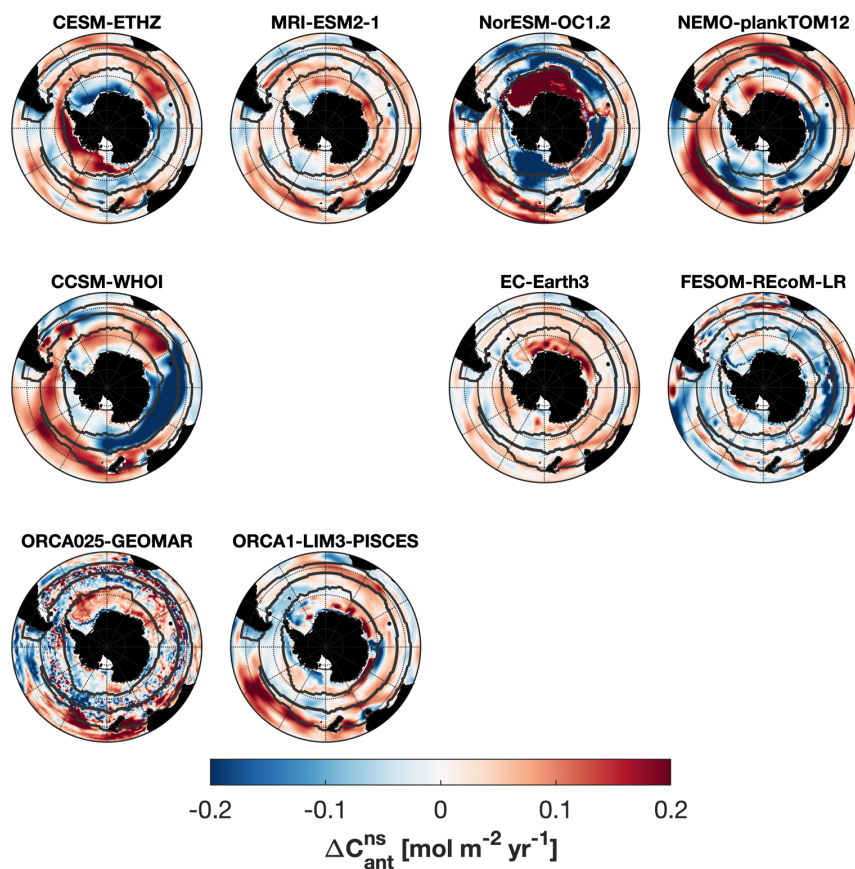
Figure S3. Non-steady state anthropogenic carbon (ΔC_{ant}^{ns}) accumulation rates over the period 1994-2007. Shown are only models where this decomposition is possible.

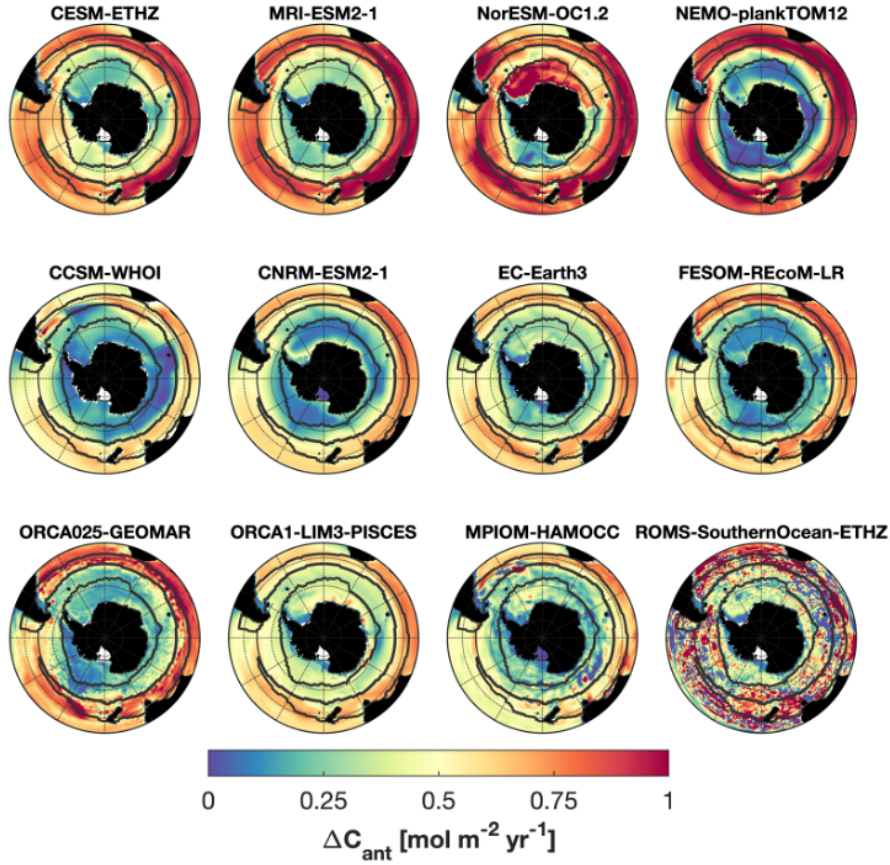**Figure S4.** ΔC_{ant} accumulation rate from 1994 to 2007 integrated to 3000 m depth for individual models. ΔC_{ant}^{tot} is shown for "GOBMs high" models CESM-ETHZ, MRI-ESM2-1, NorESM-OC1.2, and NEMO-PlankTOM12 (top row), for "GOBMs low" models CCSM-WHOI, CNRM-ESM2-1, EC-Earth3, FESOM_REcoM_LR, ORCA025-GEOMAR, ORCA1-LIM3-PISCES, and MPIOM-HAMOCC and for the regional model ROMS-SouthernOcean-ETHZ (middle and bottom rows). ΔC_{ant}^{ss} is shown for MPIOM-HAMOCC and CNRM-ESM2-1 (as justified in the main text and Text S2). Biome boundaries are shown as contours.
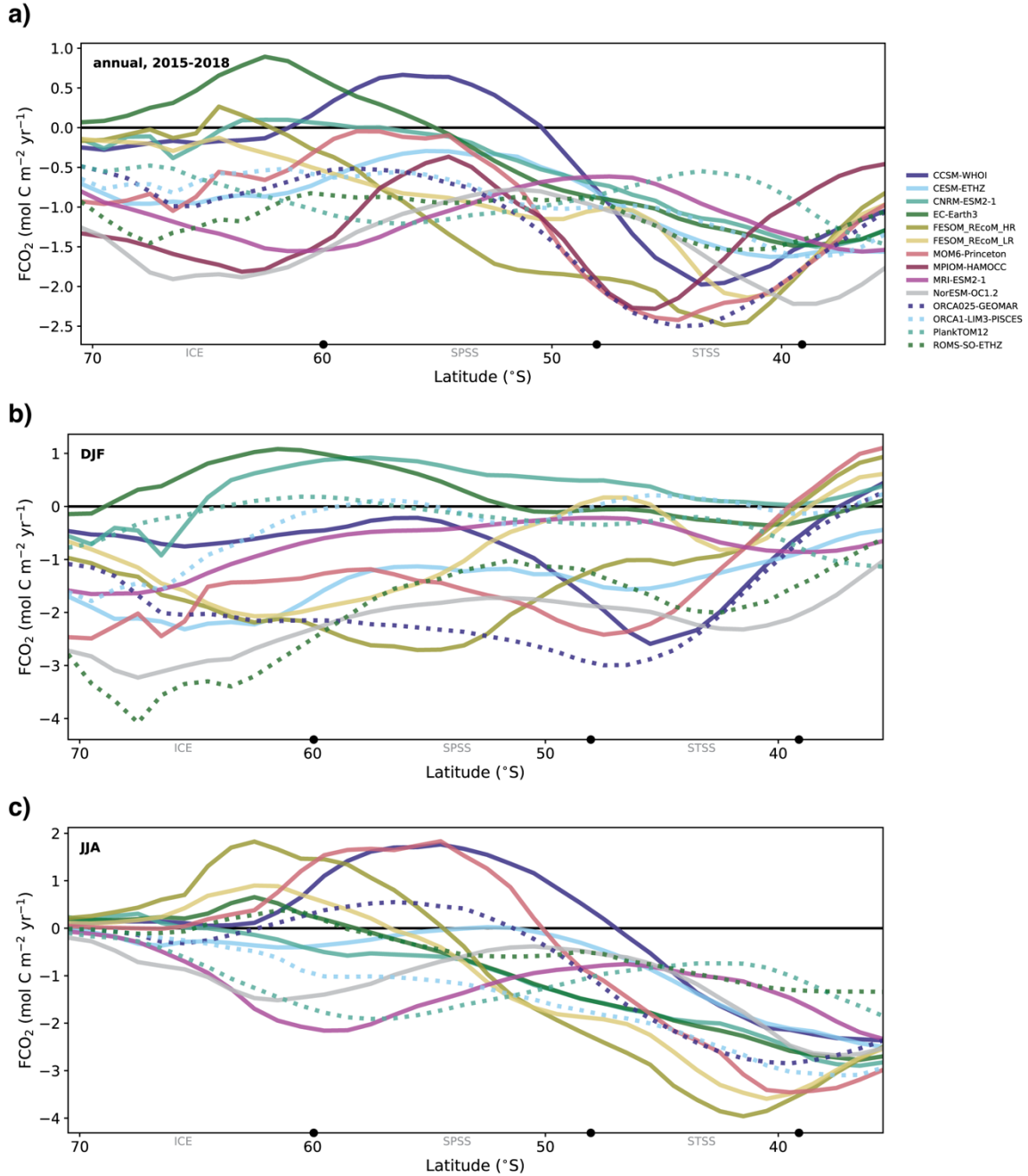
Figure S5: Zonal mean of flux density for individual GOBMs in the period 2015-2018. We show the (a) annual, (b) summer, and (c) winter zonal averages. The black markers on the x-axes show the mean location of the biome boundaries with the names of the biomes shown in gray. The MPIOM-HAMOCC model is excluded in panels b and c because of an overly strong seasonal amplitude.
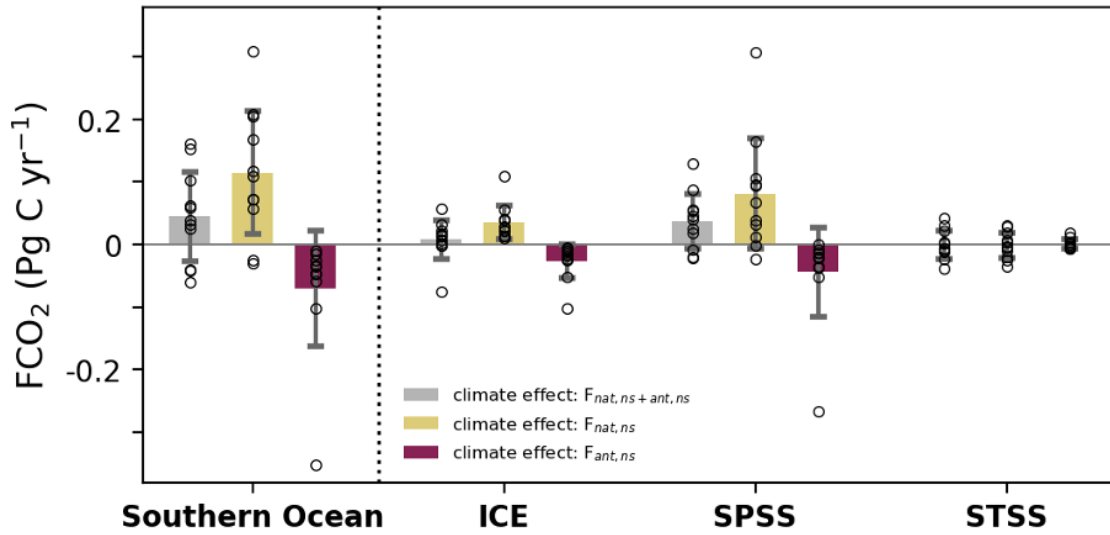
Figure S6: Same as Figure 3, but separating the total climate effect on CO_2 fluxes (gray) into the climate effect on natural (yellow) and anthropogenic (dark red) CO_2 fluxes. The climate effects on natural and anthropogenic CO_2 fluxes partly compensate each other.
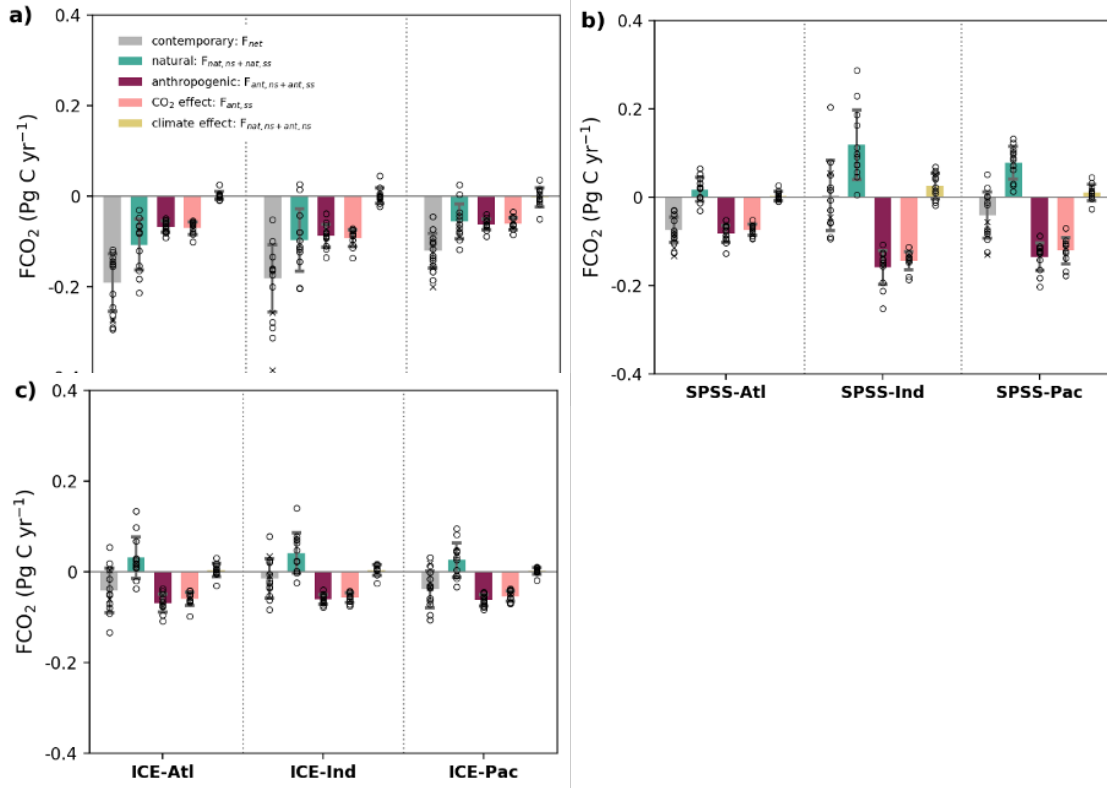
Figure S7: Same as Figure 3, but further split into Atlantic, Pacific and Indian Ocean sectors. The sub-biome-scale natural–anthropogenic decomposition of the air-sea CO_2 fluxes from the Global Ocean Biogeochemical Models in the Southern Ocean for the (a) Subtropical Seasonally Stratified, (b) Subpolar Seasonally Stratified, and (c) ICE biomes. The bars show the model ensemble mean, the circles show the individual models, and the error bars represent one standard deviation around the mean.
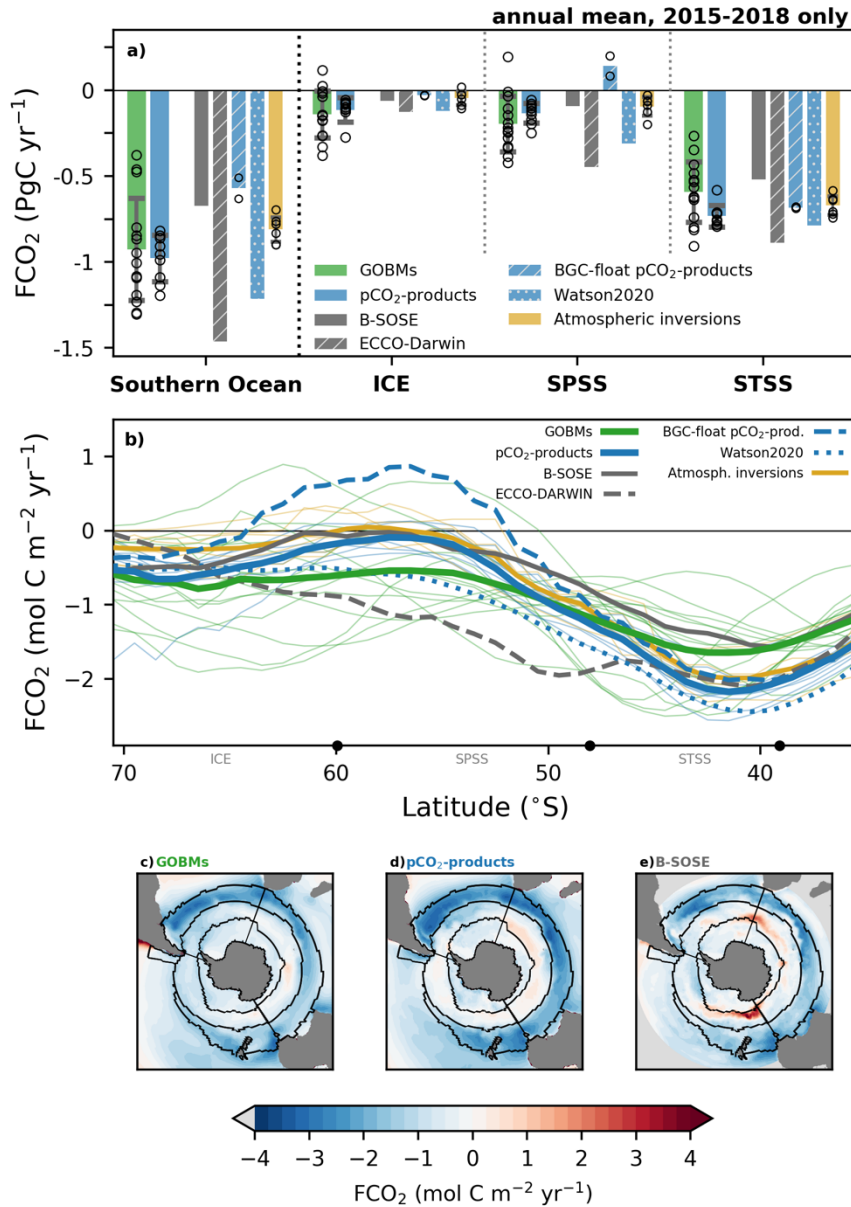
Figure S8. Temporal average of the contemporary Southern Ocean CO_2 flux (FCO_2) 2015-2018. A positive flux denotes outgassing from ocean to atmosphere. GOBMs: global ocean biogeochemistry models. (a) The green and blue bar plots show the ensemble mean of the GOBMs and pCO_2-products, and open circles indicate the individual GOBMs and pCO_2- products. The ensemble standard deviation (1σ) is shown by the error bars. The other bars show other individual estimates as indicated in the legend (see also methods), (b-d) maps of spatial distribution of net CO_2 flux for ensemble means of GOBMs, pCO_2- products and of the data-assimilated regional model B-SOSE. (e) zonal mean flux of the different data sets. Thick green and blue lines show the ensemble means, and thin green and blue lines show the individual GOBMs and p CO_2-products. Other colors as in panel a. Approximate boundaries for biomes are marked with black points on the x axis.
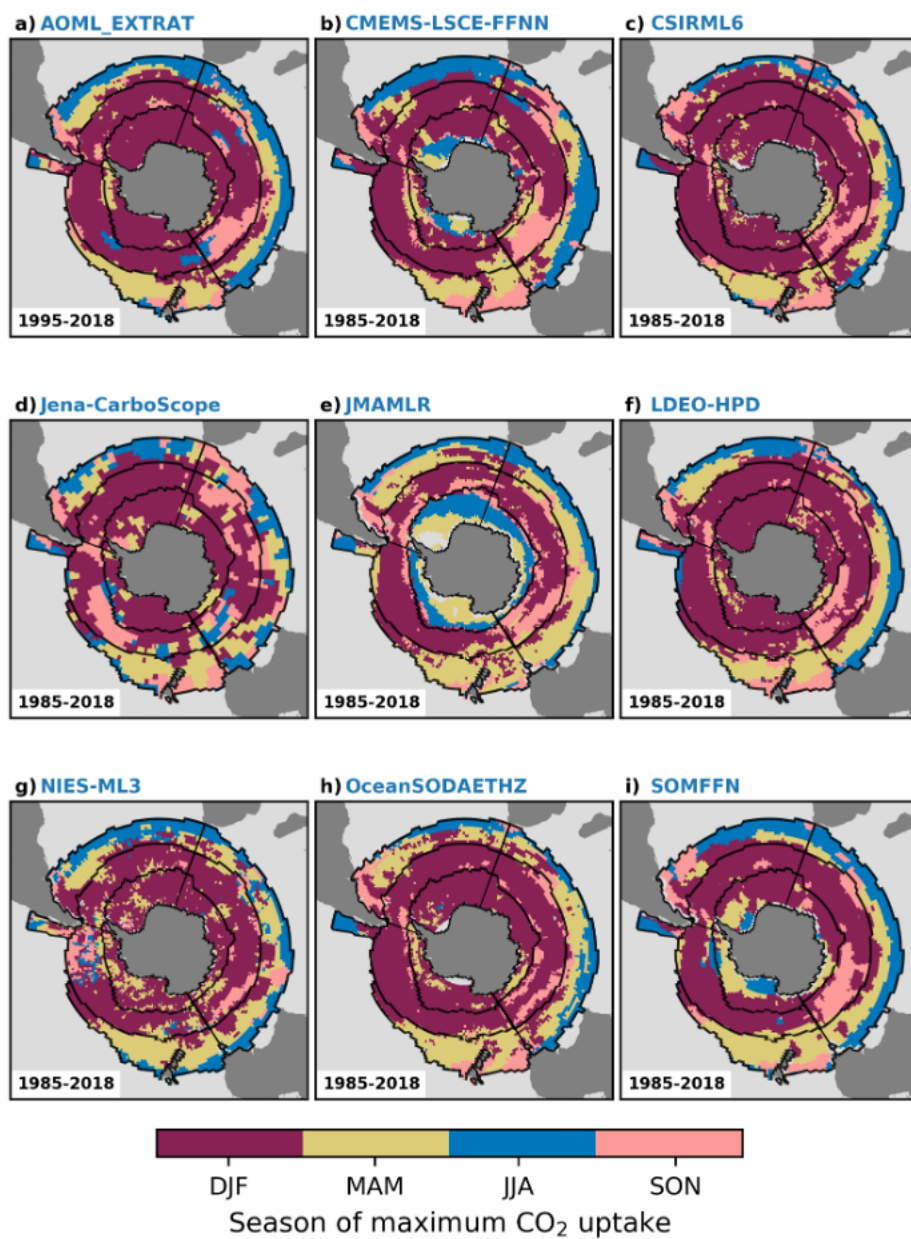
Figure S9: The season of maximum CO_2 uptake per grid cell for the pCO_2-products over the period indicated in the panels.
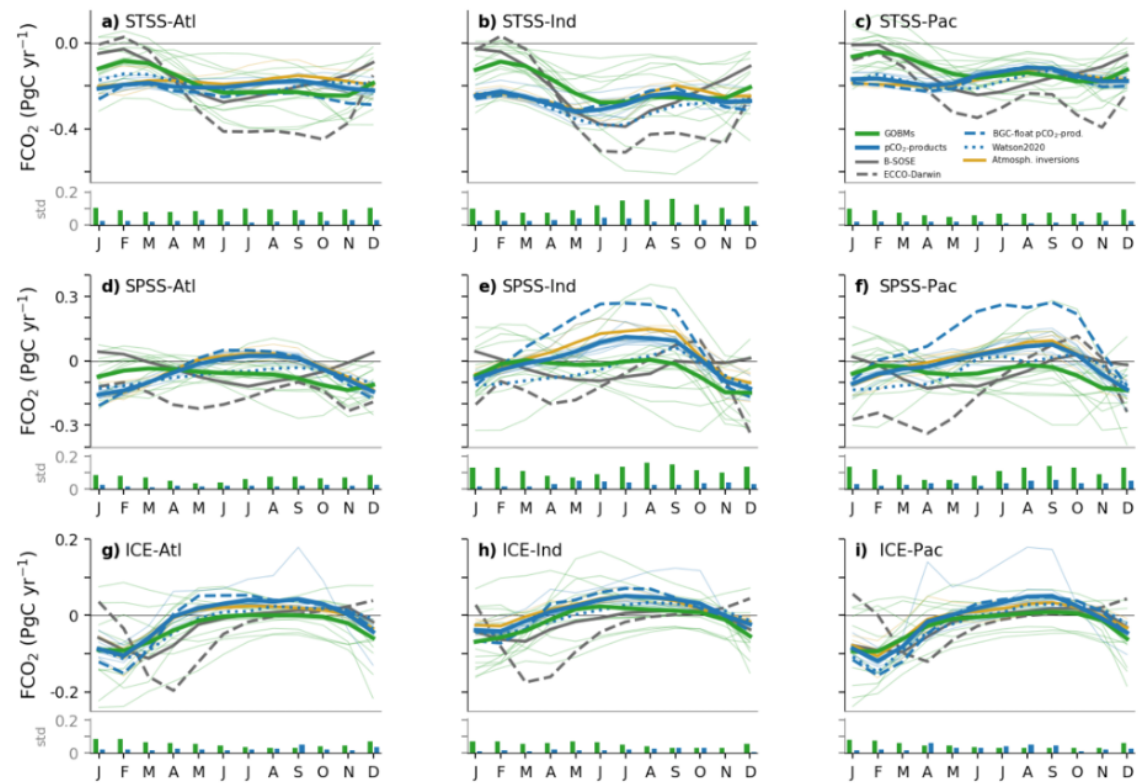
Figure S10: Seasonal cycle monthly climatology of FCO2 for the nine subregions of the Southern Ocean (see Figure 1). The top, middle and bottom rows show the STSS, SPSS and ICE biomes respectively, while the left, center and right columns represent the Atlantic, Indian, and Pacific sectors of each biome respectively. The standard deviation of the GOBMs (solid green) and pCO$_2$-products (solid blue) are shown in the narrow lower panels of each subplot. Data has not been centered to a specific year, and each dataset has the start and end years as noted in Table 1.
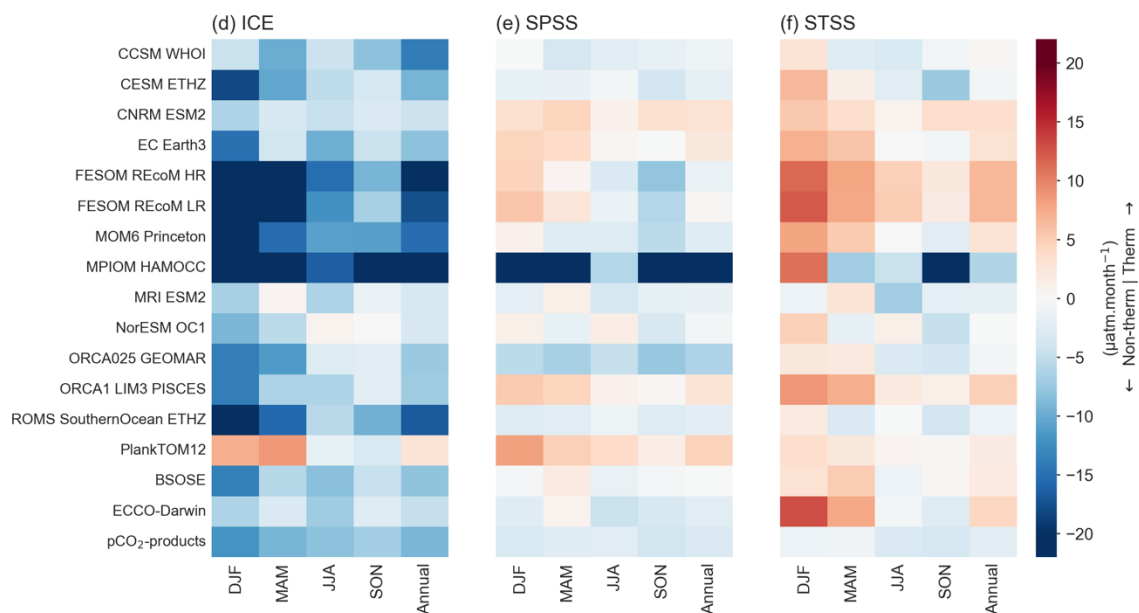
Figure S11: Same as Figure 7d-f, but showing all individual global and regional ocean biogeochemistry models and data assimilating models.
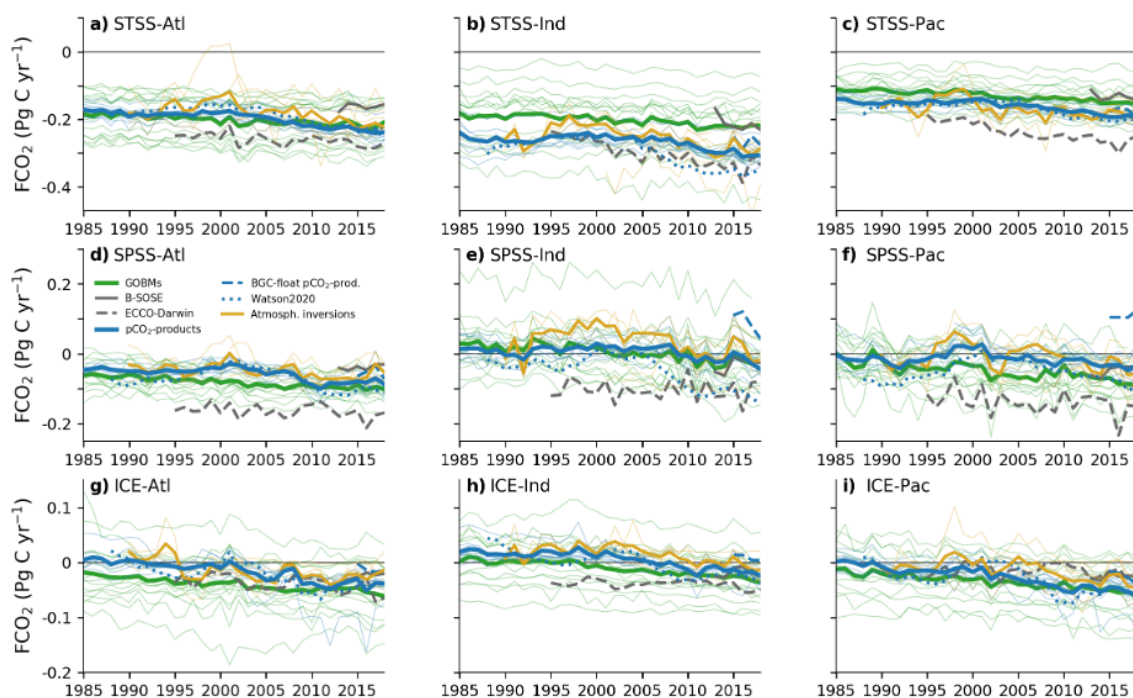
Figure S12: Same as Figure 8b-d, but further split into Atlantic, Pacific and Indian Ocean sectors of the biomes.
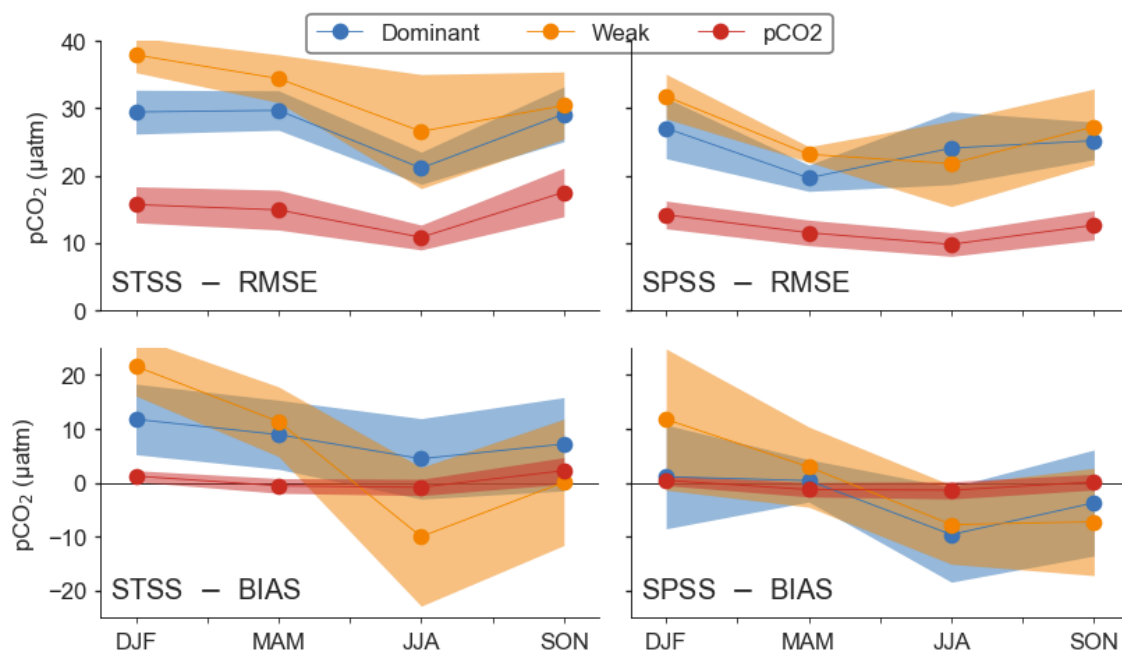
Figure S13: Comparison of surface ocean pCO_2 from DIC-dominant (blue), DIC-weak (yellow) global and regional ocean biogeochemistry models (see Table S1) and pCO_2-products (blue) to pCO2 from gridded SOCAT v2022 data set (see also Figure 9 for full Southern Ocean analysis, and section 3.3.1). Here, we calculate bias and RMSE for all observations for a given season and region. The bias is the sum of the residuals while the RMSE is the square root of the sum of the squared residuals.
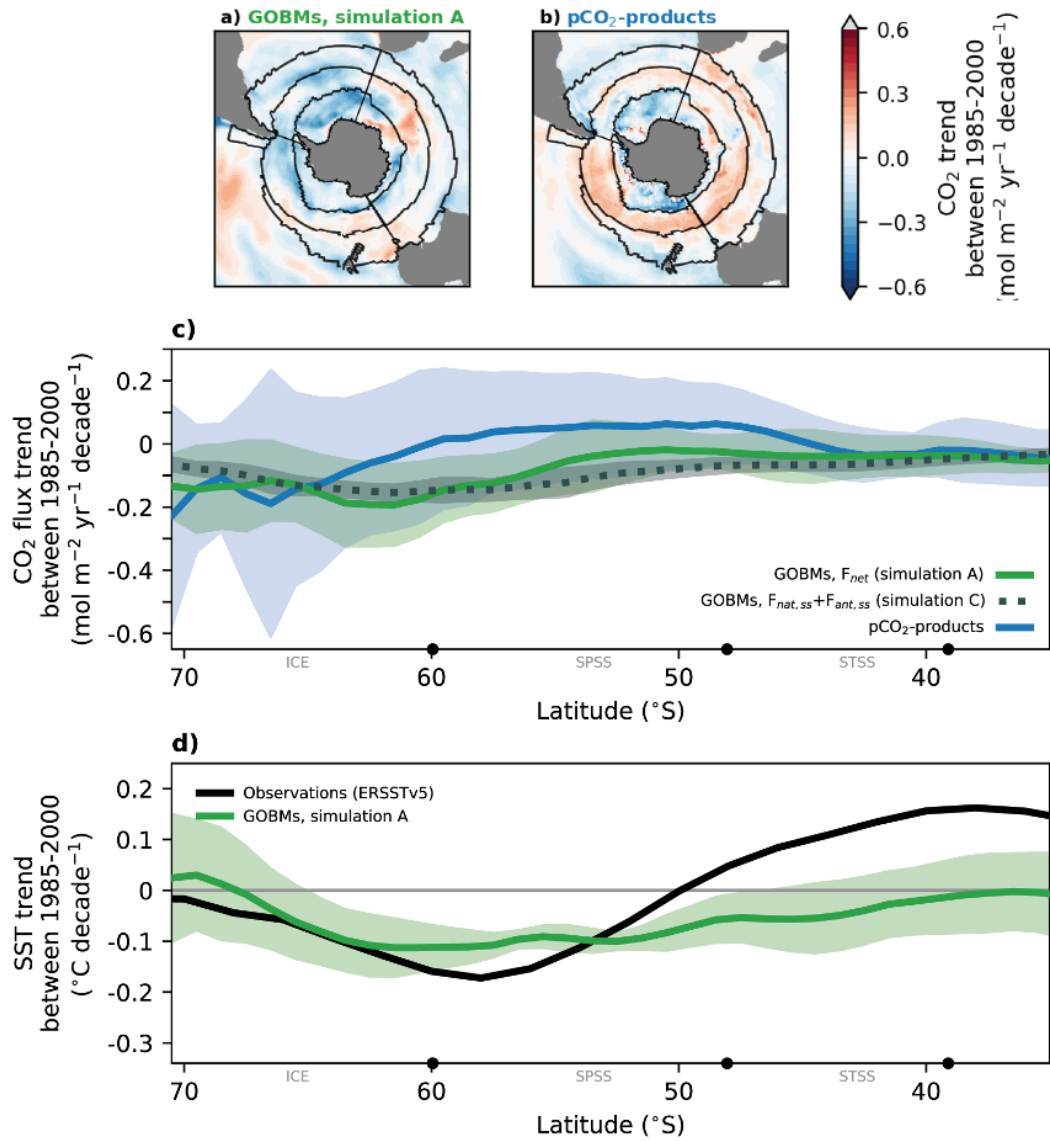
Figure S14: Same as Figure 10, but CO_2 flux trend shown here for the period 1985 to 2000. Note different scales than in Figure 10.
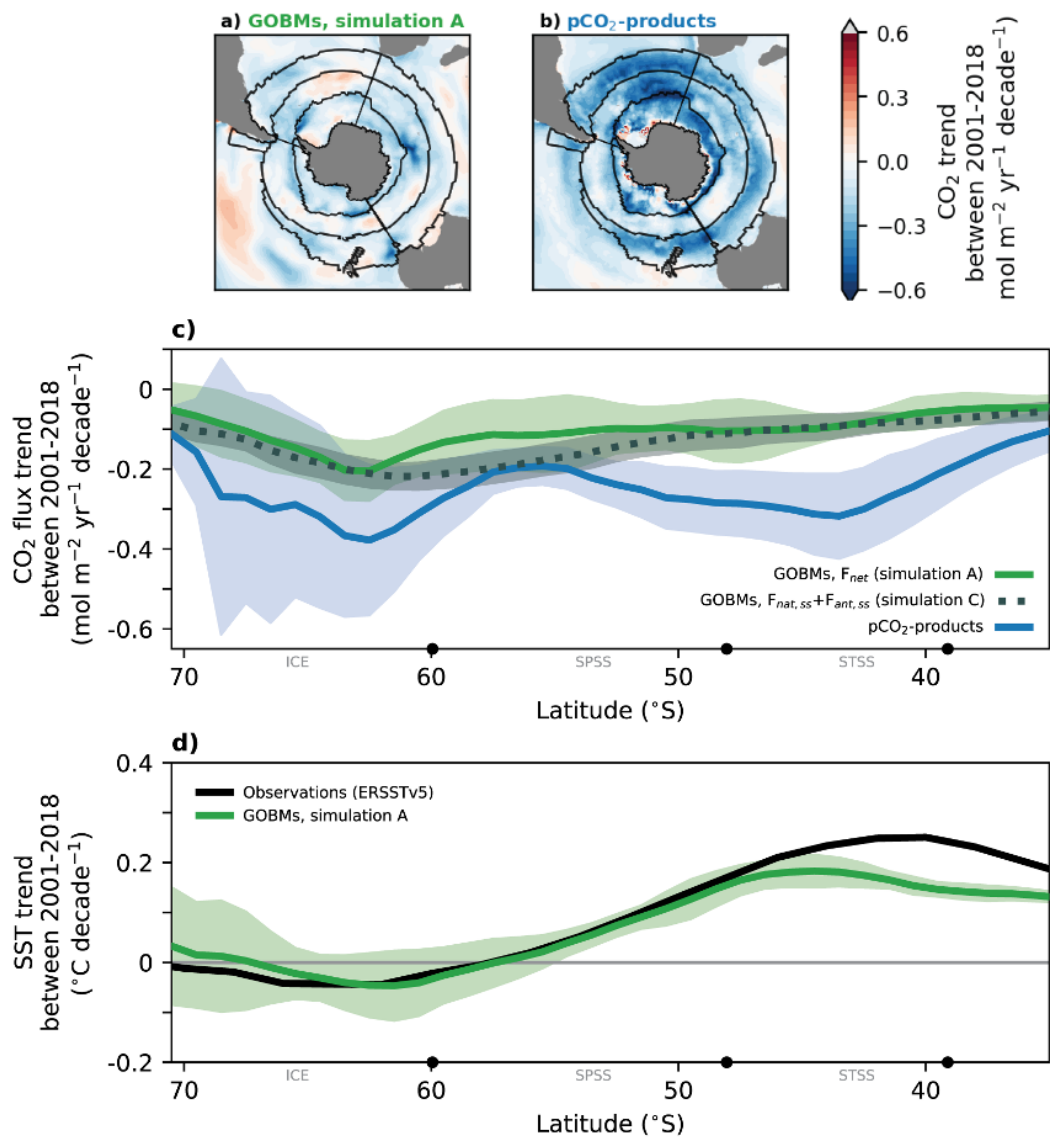
Figure S15: Same as Figure 10, but CO_2 flux trend shown here for the period 2001 to 2018. Note different scales than in Figure 10.
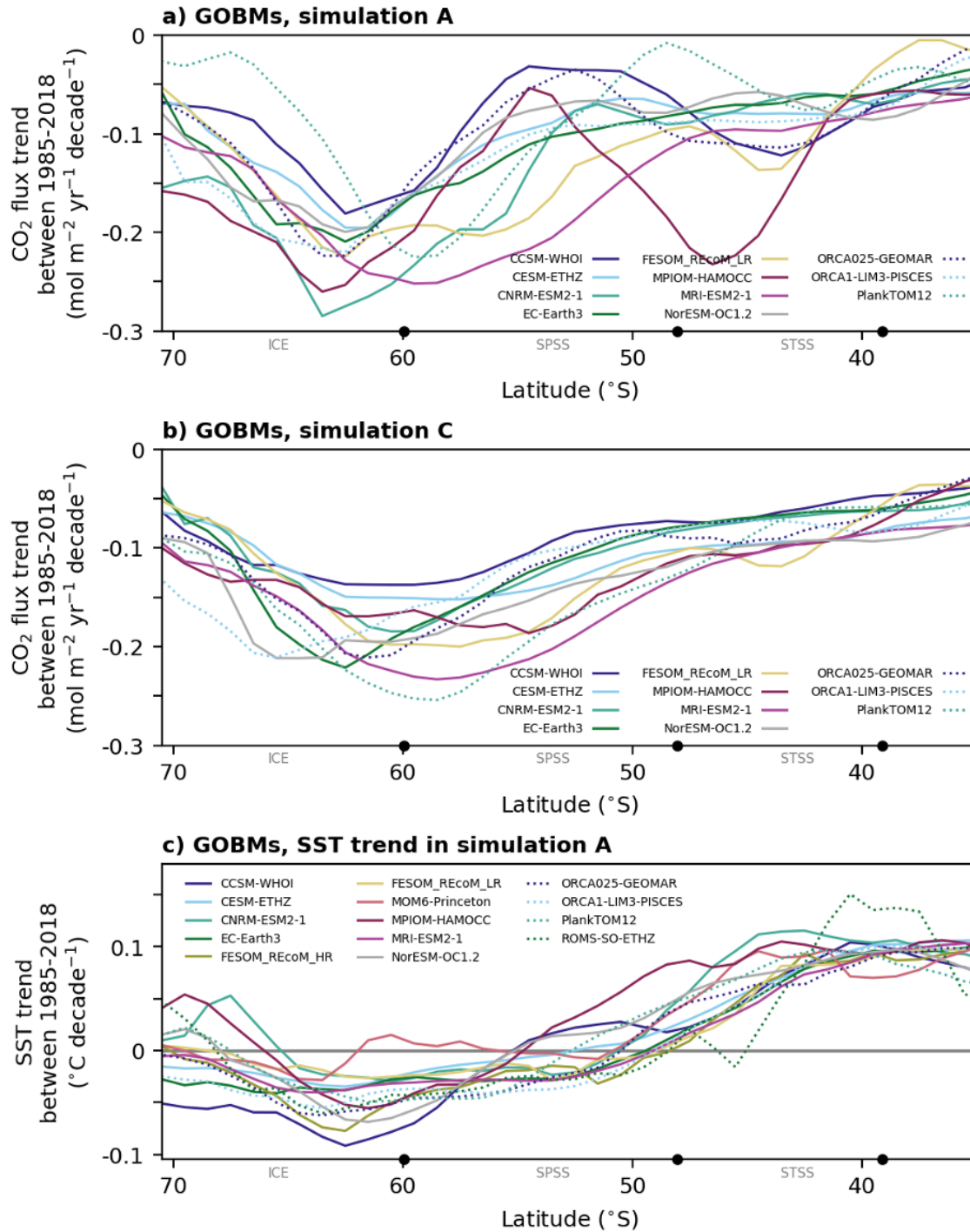
Figure S16: CO$_2$ flux and temperature trends 1985-2018 for individual models. (a) Net CO$_2$ flux trend from simulation A, (b) Steady state CO$_2$ flux trend (F$_{nat,ss}$ and F$_{ant,ss}$) from simulation, (c) sea surface temperature (SST) trend in simulation A.
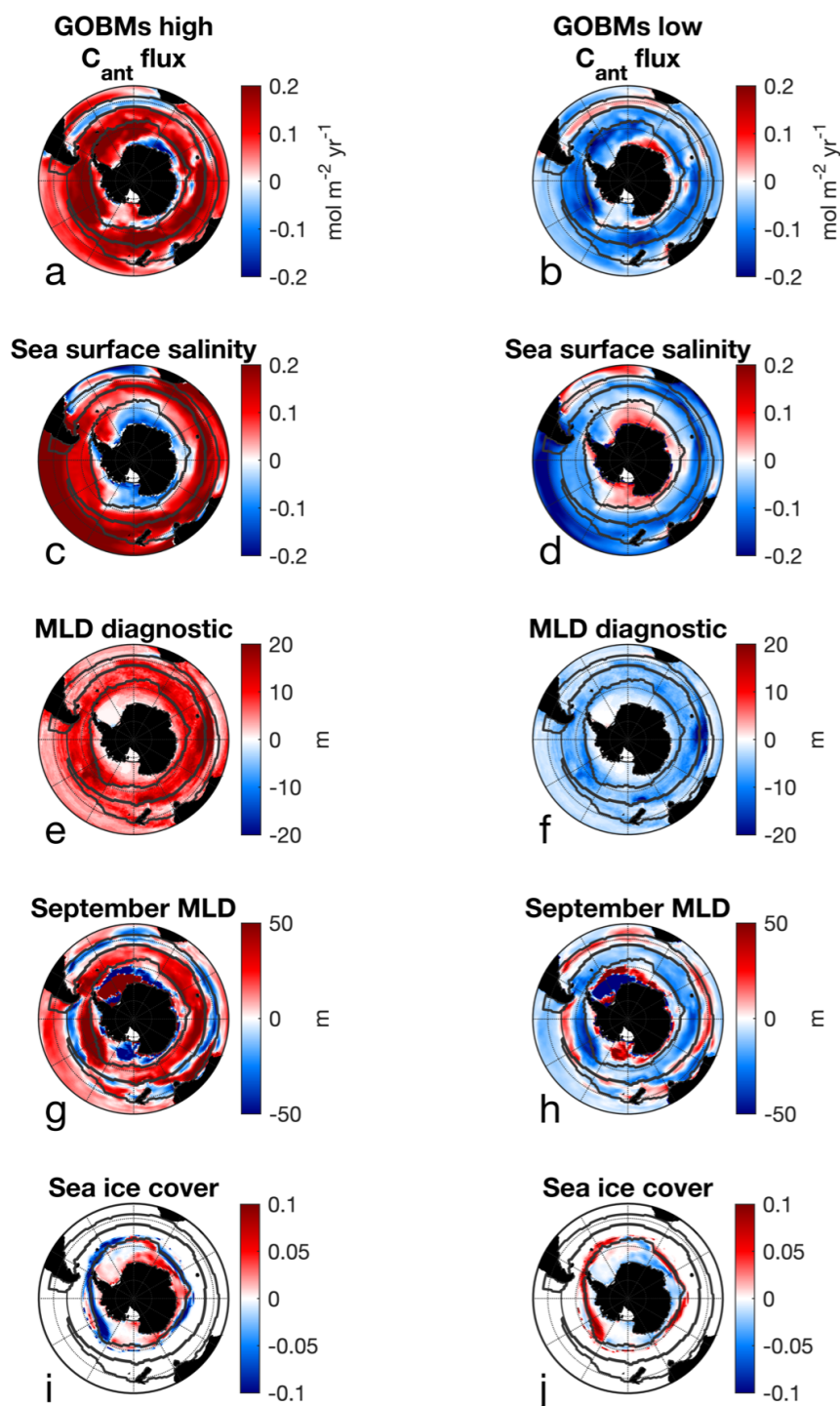
Figure S17: Composite anomalies averaged over years 1994-1007 of a,b) C_{ant} flux, c,d) sea surface salinity, e,f) MLD annual diagnostic using variable density threshold, g,h) user-defined September MLD with fixed density threshold, and i,j) sea ice concentration for models with ΔC_{ant} higher ("GOBMs high", left column) and lower ("GOBMs low", right column) than the average of the observation-based products eMLRC* and OCIM-v2021.

Shown are anomalies with respect to the multi-model-mean of these nine models. The "GOBMs high" models are CESM-ETHZ, MRI-ESM-1, NorESM-OC1.2, and NEMO-PlankTOM12. The "GOBMs low" models are: CCSM-WHOI, CNRM-ESM2-1, EC-Earth3, FESOM-REcoM-LR, ORCA025-GEOMAR, ORCA1-LIM3-PISCES and MPIOM-HAMOCC. CNRM-ESM2 was excluded from the composite analysis because it shows areas of negative ΔC_{ant} ; ROMS-SouthernOcean-ETHZ was also excluded because it has a different spin-up procedure with respect to other models (see Methods Section). The robustness of the patterns has been tested by removing in turn one model from the list. The patterns are retained even when the two models at the higher end (NorESM-OC1.2) and lower end (CCSM-WHOI) are removed from the composites. By construction, the sum of anomaly patterns in GOBMs high and GOBMs low is zero (in other words, the patterns are specular with respect to the multi model mean).
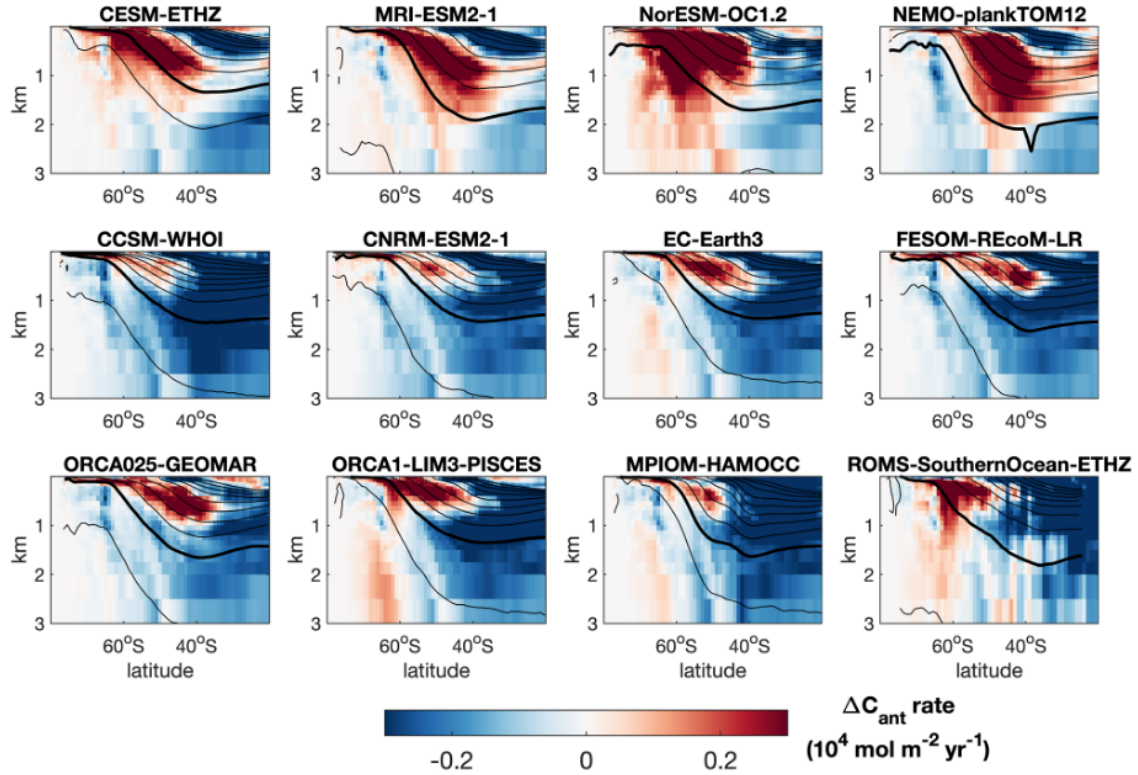

Figure S18: Anomalies, computed with respect to eMLR(C*), of ΔC_{ant} accumulation rates for the "GOBMs high" (top row) , for "GOBMs low" and for the regional model ROMS-SouthernOcean-ETHZ (middle and bottom rows). Contours show, for each model, the zonally-averaged potential density for the period 1994-2007 (with a 0.02 kg m^{-3} spacing), where the thick contour indicates the 1027.6 kg m^{-3} isopycnal.
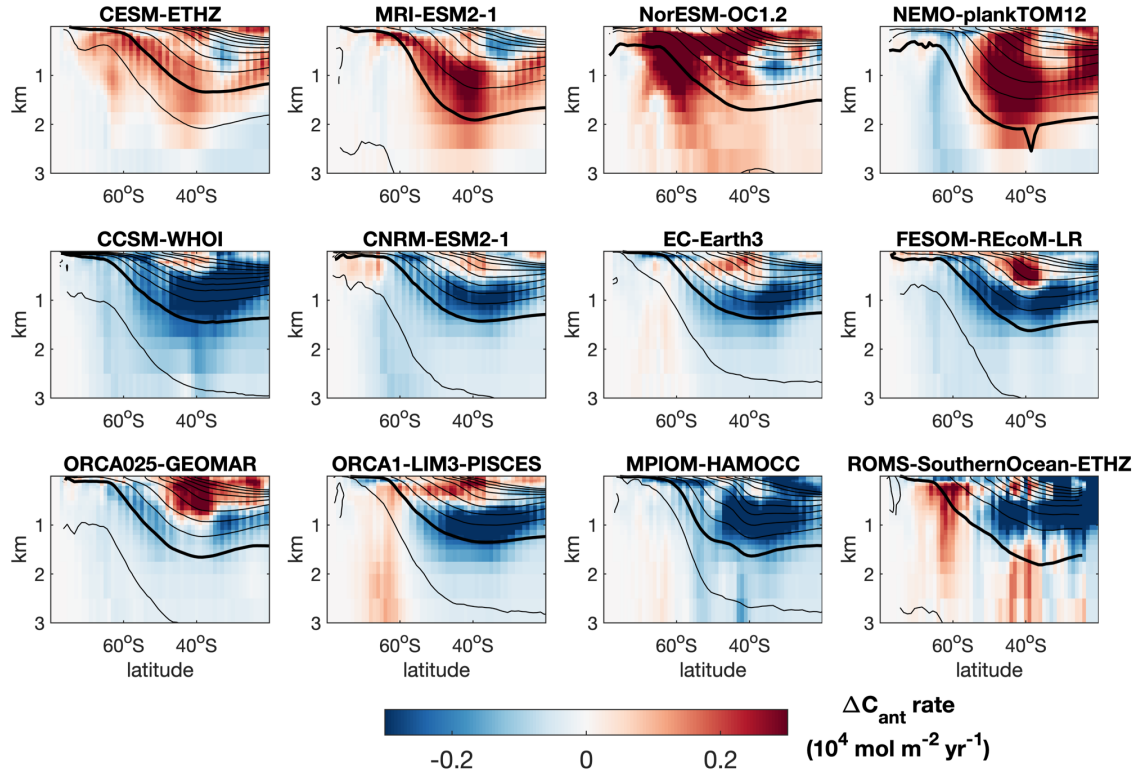
Figure S19: Anomalies, computed with respect to OCIM-v2021, of ΔC_{ant} accumulation rates for the "GOBMs high" (top row) , for "GOBMs low" and for the regional model ROMS-SouthernOcean-ETHZ (middle and bottom rows). Contours show, for each model, the zonally-averaged potential density for the period 1994-2007 (with a 0.02 kg m^{-3} spacing), where the thick contour indicates the 1027.6 kg m^{-3} isopycnal.

Table S1. Illustration of the Global Ocean Biogeochemistry Models (GOBMs) simulations A to D. Simulation A and C are forced with interannual varying atmospheric CO_2 as in historical observations, and simulations B and D are forced with constant (preindustrial atmospheric CO_2. Climate forcing varies interannually in simulations A and D, and a repeated single year or multi-year climatology is used in simulations B and C. F_{net}: net air-sea CO_2 flux. Flux components: C_{ant}: anthropogenic carbon, C_{nat}: natural carbon, ss: steady state, ns: non steady state. See main text for explanation.
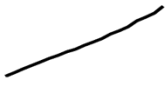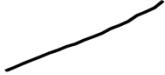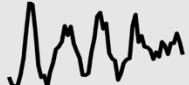
	CO₂atm	Climate forcing	Flux component

A — $F_{net} = C_{ant}^{ss} + C_{ant}^{ns} + C_{nat}^{ss} + C_{nat}^{ns}$

B — C_{nat}^{ss}

C — $C_{ant}^{ss} + C_{nat}^{ss}$

D — $C_{nat}^{ns} + C_{nat}^{ss}$

Table S2. Refers to the classification of models in Figure 7 into those that have a strong or weak DIC seasonal cycle contribution to pCO_2. We refer to these as DIC dominant or DIC weak rather than thermal or non-thermal as the thermal contribution is relatively similar for all models as the RECCAP2 models use atmospheric forcing, resulting in well-constrained temperature contributions.

	Global and regional ocean biogeochemistry models
DIC dominant	CCSM WHOI, CESM ETHZ, MRI-ESM2, NorESM-OC1, ORCA025-GEOMAR, ROMS-SouthernOcean-ETHZ
DIC weak	CNRM-ESM2, EC-Earth3, FESOM-REcoM-HR, FESOM-REcoM-LR, MOM6-Princeton, ORCA1-LIM3-PISCES, PlankTOM12